



Waste to Resource: Surface Modification of Electric Arc Furnace Flue Dust by Ball Milling and In Situ Carbonization

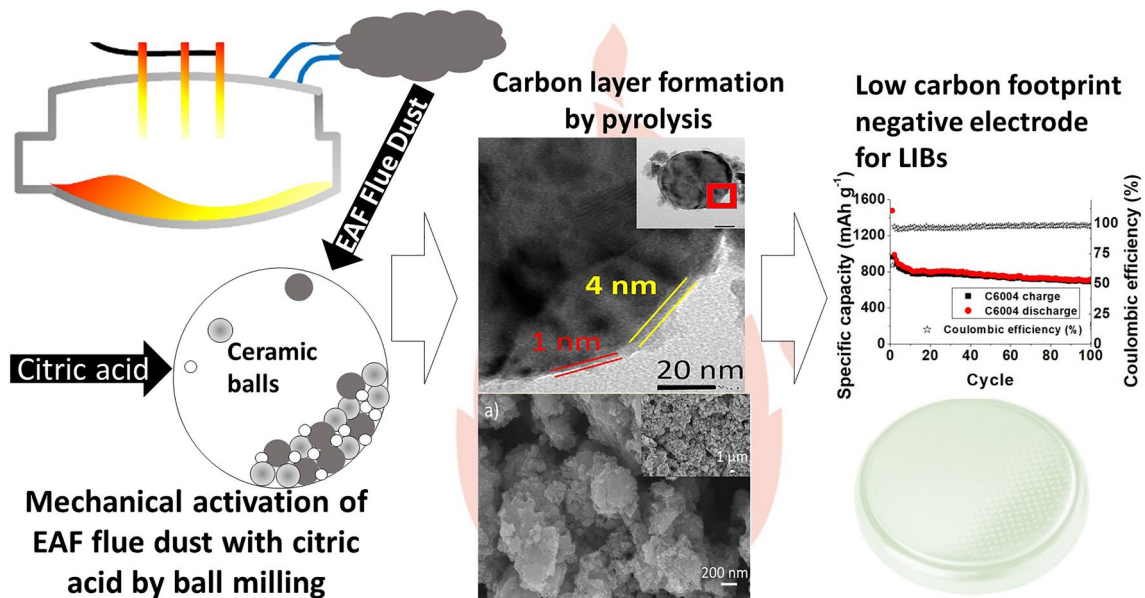
Mehmet Feryat Gülcan¹ · Billur Deniz Karahan^{1,2}

Received: 23 June 2023 / Accepted: 25 January 2024
© The Author(s) 2024

Abstract

In this article, instead of synthesizing the electrode active material using expensive precursors that lead to high carbon emissions to the atmosphere during fabrication, an alternative engineering approach is presented for the utilization of the electric arc furnace flue dust, which is an industrial waste, as anode material in lithium-ion batteries. In this scope, firstly ball milling of the flue dust with citric acid is applied and then in situ carbonization conditions are optimized by pyrolyzing the mixture at different temperatures (600 °C and 750 °C) and times (4 h and 6 h). Every sample delivers capacities greater than graphite. Structural, morphological, and chemical characterization results demonstrate that the designed method not only promotes the formation of a nanometer-thick carbon layer formation over the particles but also induces partial phase transformation in the structure. The best performance is achieved when citric acid is used as the carbon source and the ball-milled powder is treated at 600 °C for 4 h in nitrogen (C6004): It delivers 714 mAh g⁻¹ capacity under a current load of 50 mA g⁻¹ after 100 cycles. This research is expected to set an example for the utilization of different industrial wastes in high value-added applications, such as energy storage.

Graphical Abstract



Keywords Electric arc furnace flue dust · Pyrolysis · Lithium-ion battery · Waste valorization · Low carbon footprint C-coated electrodes · Planetary ball mill

The contributing editor for this article was Zhi Sun.

Extended author information available on the last page of the article

Introduction

Fossil fuels used to produce energy are no longer favored because of their significant carbon dioxide emissions, which harm the environment [1]. As a result, the use of renewable energy sources is strongly encouraged, which calls for the efficient use of energy storage technologies. Among alternatives, lithium-ion batteries (LIB) are preferred because they do not have a memory effect, can operate at high voltages, and have a high specific energy density [2]. Today, many manufacturers prefer lithium-ion batteries in electric vehicles and portable devices [2]. The use of LIB has been growing significantly over the last 10 years, and research for further improvements in performance at a cheaper price is still in demand. It has been stated that battery prices at pack level have decreased by 97% in 2020 since its first commercialization in 1991. In the same study, it was also mentioned that the expected cost per kWh in 2030 was 75 USD [3]. This situation necessitates the development of battery chemistry [4–7]. Therefore, projections show that the progress in battery technology will extend their usage, hence their production in future. When the rate of CO₂ equivalent gas released during battery production is taken into account, it is found that the active material synthesis is responsible for 54% of the total emission [8], while the cost to synthesize electrode material represents 43% of the total cost to produce batteries that store 100 kWh energy.

In this context, the assessment of industrial wastes becomes compelling as their replacement for synthetic precursors enables the utilization of easily accessible cheap material in the fabrication. Considering the environmental and financial benefits of waste evaluation during electrode fabrication, scientists have recently utilized a variety of bio-waste and industrial waste as raw materials in the fabrication [9, 10]. However, most of these studies entail selective material recovery by leaching the waste with potent chemicals. Therefore, new waste is produced during the recovery which creates the need for additional disposal procedures. Unlikely, in this work, a new method is anticipated to evaluate the entire industrial waste in a high value-added application: batteries. According to Gao et al. [11], 1 ton anode active material production causes 5315.91 kg CO_{2-eq} as this amount of production needs 112.48 GJ energy consumption. Thus, the evaluation of a waste with no economic value as active material led to less energy consumption in fabrication hence less CO₂ emissions [12].

According to the World Steel Association, the total amount of steel produced in 2021 is ~ 1.9 billion tonnes [13] and around 29% of the steel production was realized by electric arc furnace furnaces (EAF) [14]. During the

production of one ton of steel by EAF, approximately 20 kg of flue dust is formed [15]. Previous researches reveal that EAF flue dust (EAFFD) mainly contains zinc (as zincite or franklinite), iron (as franklinite), and other metals, such as Ca, Mn, Cd, and Pb [15]. Researchers have designed methods to selectively recover zinc oxide and zinc over the last few years [9, 16–19]. The main motivation of this study is to evaluate the EAFFD as electrode materials, since the uses of synthetically manufactured franklinite [20] and zincite [21] have already been examined as anode materials and their performances are found to be promising. Moreover, EAFFD has a trace amount of other metals, such as Mn, that could promote electrochemical performance by doping effect [9]. In our previous study, with the help of the knowledge of electrochemistry and metallurgy, carbon-coated electric arc furnace dust has been prepared by combining wet chemistry with one-pot pyrolysis where sucrose was used as a carbon source [22]. As the results are found to be promising, in this research first time in the open literature, a combination of ball milling with pyrolysis has been studied where citric acid is chosen as a carbon source in milling, and the pyrolysis at different conditions (temperatures and durations) have been realized to optimize the cycle performance of the anode material. Thus, by combining mechanical activation with the subsequent high-temperature thermal treatment process, a versatile technology with significant scale-up potential has been achieved [23].

In this research, the main goal of using the ball mill is to increase the interaction between the flue dust and the carbon source. As Nzabahimana et al. [24] have reported in milling, the reactants are brought together, and the powders are trapped between the colliding balls and undergo deformations that define the final powder structure. During the process, the chemical bonds of the crushed powder are broken due to the kinetic energy applied by balls, and both the particle size as well as the crystal structure change. In the experiments, a mechanical activation is realized by ball milling a suitable organic substance with the EAF flue dust. Herein, citric acid is selected because of its low oxygen content and low decomposition temperature [25]. Such interaction between two powders (i.e., citric acid and EAF flue dust) followed by a heat treatment in an oxygen-free atmosphere is expected to promote a partial phase transformation, which is accompanied by the generation of a thin carbon layer over the EAFFD.

Up to now, the production of high-performance composites by citric acid has been studied extensively in the literature (coating with magnetic stirrer, spray pyrolysis, etc.) [26, 27]. The electrochemical performance of the as-synthesized samples, however, was the focus of the majority of the studies, and unfortunately, the synthesis process received very little attention. Such knowledge, on the other

hand, is very critical for further optimizing material properties. The production of composite powder using a mechanical activation procedure with citric acid as the carbon source was thoroughly explored in this study. It is anticipated that during the mechanical activation process, active edges are formed on the dust (EAFFD), while citric acid is broken down into smaller chains. This fact partially disturbs the stable structure of the flue dust; hence, the fragmented citric acid will react more efficiently with the high-energy regions of the flue dust. Then, in the pyrolysis process applied in the next step, an amorphous carbon film is formed over the dust. During the experimental study, the pyrolysis temperatures are chosen by paying attention to the temperature values at which the carburization of citric acid is realized efficiently, but the zinc oxide from the flue gas dust would not evaporate completely.

Although the studies carried out so far have shown that the composites obtained by mechanical alloying have long cycle life at low current loads, it has been observed that such electrodes generally degrade at high current loads. With the design made in this study, it is observed that the electrode exhibits good retention over the 100th cycle and a higher capacity than graphite over 400 cycles when it is tested under a current load of 1 A g⁻¹.

Experimental

Materials

EAFFD was received from the industry. Citric acid was purchased from Merck (for analysis, %99.5–100.5). The ethanol used in this work was a technical grade from a local producer.

Material Preparation

Firstly, EAFFD was cleansed at 80 °C for 30 h with deionized water and then dried in air for 16 h at 100 °C. Afterward, 1.75 g of washed EAFFD and 1.75 g of carbon source (citric acid) were planetary ball milled where 24.5-ml ethanol was added as a dispersant. The volume of the vial was 500 ml and ball-to-powder ratio (wt/wt) was 40:1. The vial and balls were made of zirconia and the balls radius is 5 mm. Planetary ball milling was performed at 400 rpm for 5 h with 20-min ON and 10-min OFF mode to minimize the overheating problem (Retsch PM100). Then, the obtained powder was dried at 80 °C in a vacuum for 16 h. Pyrolysis was realized when the dried powders were treated in a nitrogen atmosphere: C6004 (citric acid-milled powder pyrolyzed at 600 °C for 4 h), C6006 (citric acid-milled powder pyrolyzed at 600 °C for 6 h), and C7504 (citric acid-milled powder pyrolyzed at 750 °C for 4 h).

Material Characterization

X-ray fluorescence was used to examine the chemical composition of the EAFFD (Table 1) after cleaning at 80 °C for 30 h with deionized water (Hitachi X-MET8000). Scanning electron microscopy was used to examine the morphologies of the powders (C6004, C6006 and C7504) (SEM, Zeiss Gemini 500). Raman spectra of the samples (EAFFD, C6004, C6006, and C7504) were collected for 5 min at room temperature using a micro-Raman spectroscope (Renishaw, 532). 1 μm diameter He–Ne laser with a 50 × 50 micron objective was used to evaluate carbon bond type in the composites. Analyses were conducted 3 times in the same area to verify data reliability.

Eltra CS800 was used to quantify the amount of carbon in each sample.

The structural investigations were performed by X-ray diffractometer (Bruker AXS/Discovery D8) between 2θ = 20°–70° with a scanning rate of 1°/min using a Cu Kα source. The JEOL TEM 2100 was used to conduct a High-Resolution Transmission Electron Microscopy (HRTEM) study on the C6004 sample (LaB₆, 200 kV). Oxford 80 T performed the EDX analysis.

Electrochemical investigation

Firstly, the active material was intimately combined with Timcal-C64 and polyvinylidene fluoride (PVDF: MTI HSV900) dissolved in N-methyl-2-pyrrolidone (NMP: Merck) with an 80:10:10 weight ratio. The slurry preparation was done by Thinky ARE-250. Then, the slurry was laminated on a current collector made of 10-μm-thick copper foil (> 99.90 purity). The laminations were calendared, punched, and weighed after being dried in a vacuum at 120 °C for 16 h.

CR2032 standard half-cells were built in a glovebox (MBRAUN, Labmaster with < 1 ppm O₂, < 1 ppm H₂O) to test the performance of each electrode. The counter electrode was lithium, the separator was a Celgard 2400, and the electrolyte was Merck grade solution formed of 1-M LiPF₆

Table 1 XRF analysis of Pristine EAFFD

Element	Percentage (%)
Si	0.28
S	0.22
Mn	3.04
Fe	27.35
Zn	68.2
W	0.25
Cr	0.19
Ta	0.34
Pb	0.12

dissolved in EC: DMC (1:1). With Gamry Interface 1000E, electrochemical impedance spectra (EIS) of C6004 and the pristine EAFFD were collected. Impedance measurements were realized with symmetric cells, as Chen et al. [28] suggested to avoid any effect caused by the impedance of Li metal present in the half-cell. To measure EIS with symmetrical cells, firstly, two half-cells were assembled from the same electrode and discharged down to 1 mV vs Li. Then, both cells were polarized (at 1 mV) for 16 h until the current passing through each cell became lower than $C/100$. Then the two cells were taken to the glove box and disassembled there. The working electrode (here in 'anode') of each half-cell was removed and a new cell was assembled from the two electrodes being polarized to 1 mV. This newly assembled symmetric cell was kept in the glovebox overnight and an EIS test was applied with 1-mV rms stimulation.

Finally, as proposed by Duan et al. [29], a sweep voltammetry approach was utilized to study the capacitive contribution to the overall lithium storage capacity of C6004 (vs the pristine EAFFD) when the samples were cycled between 1 mV and 3 V at different sweep rates: 0.3, 0.5, 1, and 1.5 mV s^{-1} . Herein, to avoid the effect of the irreversible

reaction that occurred at the beginning of the cycling test, first, the half-cell had been cycled 3 times galvanostatically and then the sweep voltammetry analysis result of each electrode was recorded.

Results and Discussion

Material Characterization

XRF analysis of the EAFFD after being washed with water for 30 h shows that (Table 1) it contains a high amount of zinc (68.2%) and iron (27.35%) akin to the literature [9]. SEM images reveal that after washing with water, particles of different sizes and shapes are noted similar to those presented in our previous work [22]. After milling and pyrolysis, surface irregularities are noted around each particle which is believed to be related to carbon film formation. When comparing SEM pictures (Fig. 1a–b) of C6006 to C6004, longer calcination duration (C6006) is noted to promote agglomeration [30]. Then, when SEM images

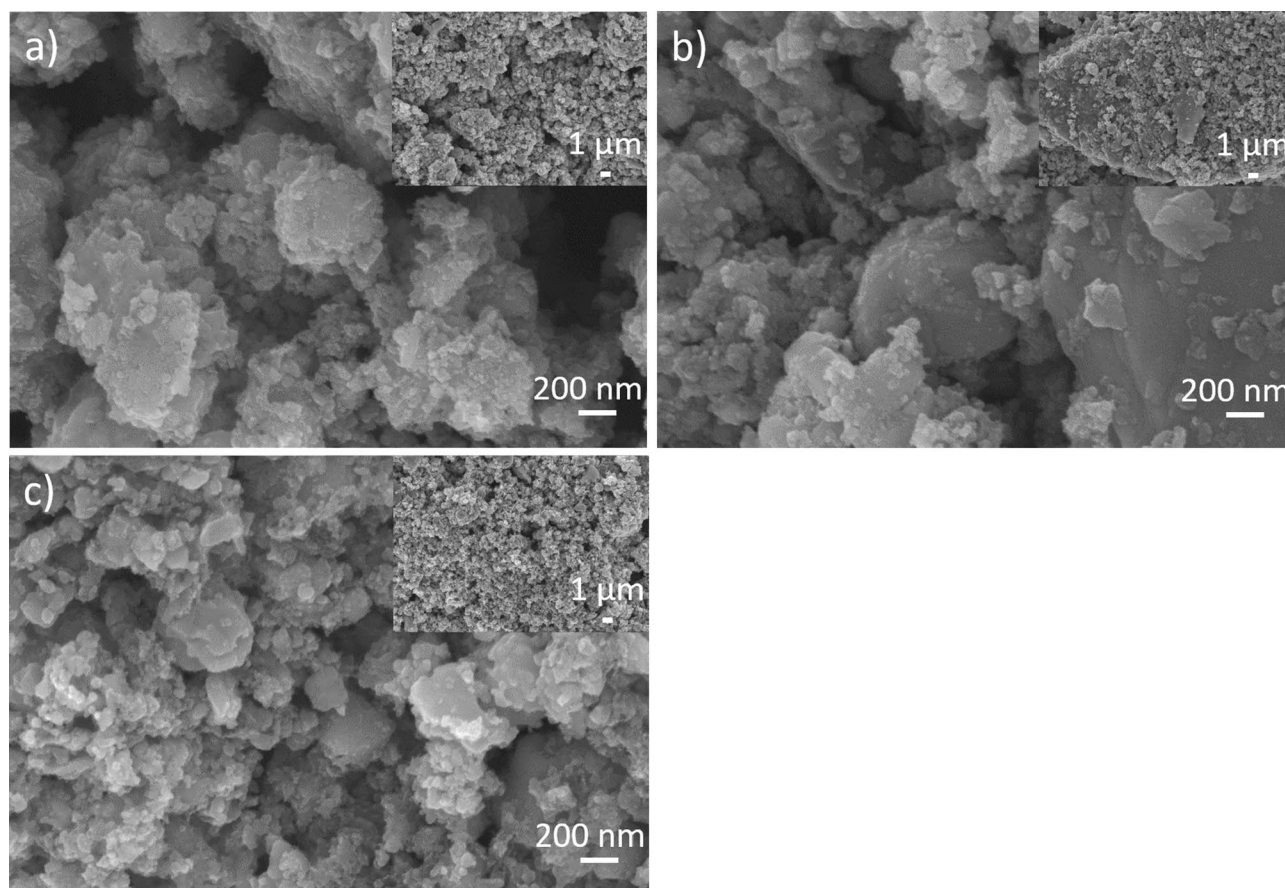


Fig. 1 SEM images of **a** C6004, **b** C6006, and **c** C7504

(Fig. 1c–a) of C7504 and C6004 are compared, the particle size is found to be decreased at higher temperature.

XRD analysis of each sample is given in Fig. 2. In the case of pristine EAFFD, typical phases (such as franklinite, zincite, calcite, and iron oxides) are found akin to the literature [22, 31, 32]. By applying planetary ball milling, a homogeneous mixture of EAFFD with citric acid is provided at the defined experimental conditions, then via pyrolysis at different temperatures and durations phase transformation is achieved with different efficiencies. As a result, Fig. 2 reveals that some phases disappear and new phases form in C6004, C6006, and C7504 [33], eventually after the pyrolysis step (see Supp. Figures S1–S3 for detailed XRD analysis).

When a scrutiny investigation on the effect of carbon coating is studied (C6004 in comparison to the pristine (i.e., ‘non-coated EAFFD’) seen in Fig. 2 and online supplementary Figure S1), it is seen that the peak intensities of the calcite (at $2\theta = 29.46^\circ$) and franklinite ($2\theta = 29.93^\circ$) are decreased, while new peaks related to maghemite formation appear ($2\theta = 30.24^\circ, 50.43^\circ, 59.98^\circ, \text{ and } 62.91^\circ$). Moreover, peaks related to hematite disappear ($2\theta = 33.39^\circ$) and a remarkable peak shifting is noted in zincite ($2\theta = 31.84^\circ, 34.49^\circ, 36.27^\circ$), which can be explained by the fact that under the defined heat treatment conditions, C atoms reduce oxides to some extent and reduced metals may partially diffuse into ZnO crystal causing deformation in its structure. Then, by comparing the XRD data of the C6006 with the pristine (Fig. 2 and Figure S2), the effect of pyrolysis at a longer duration is discussed: peaks related to calcite ($2\theta = 29.46^\circ$) and hematite ($2\theta = 33.39^\circ$) disappear, while new peaks related to maghemite formation appear ($2\theta = 30.35^\circ, 60.24^\circ$). Moreover, the intensities, as well

as the number of peaks related to franklinite ($2\theta = 29.93^\circ, 53.21^\circ, 62.34^\circ$) are decreased. Herein, the fact that the peaks intensities of ZnO are decreased (C6006 vs pristine EAFFD) could be related to partial ZnO evaporation at longer pyrolysis duration. Then, the fact that the peak shifting in ZnO becomes less remarkable in C6006 (vs C6004) may be related to the enhanced diffusion of atoms at a longer duration, leading to a more stable structure formation with larger particle size.

When the effect of the high pyrolysis temperature on the composite powder’s structure is studied (C7504 vs the pristine), peaks related to calcite ($2\theta = 29.46^\circ$) and hematite ($2\theta = 33.39^\circ$) are found to disappear, and new peaks related to maghemite ($2\theta = 30.35^\circ, 60.24^\circ$) and wuestite ($2\theta = 42.36^\circ, 61.40^\circ$) are recognized. Additionally, the intensities, as well as the number of peaks related to franklinite ($2\theta = 29.93^\circ, 35.28^\circ, 42.88^\circ, 53.21^\circ, 56.67^\circ$) are remarkably decreased, similar to C6004 and C6006. However, unlike others (C6004, C6006), C7504 depicts less number of zincite peaks (at $2\theta = 31.84^\circ, 34.49^\circ, 47.55^\circ, 68.08^\circ, 69.15^\circ$ disappear) as reported by Holloway et al. [34] and Wu et al. [35]. Such a remarkable change is believed to be related to the different phase transformation occurring at different pyrolysis temperatures.

The studies examining the thermal decomposition of citric acid in a nitrogen atmosphere show that the maximum rate of weight loss is found to occur at $180\text{--}200^\circ\text{C}$ [36] and the carburization reaction changes upon the temperature: at lower temperatures ($T < 700^\circ\text{C}$), pyrolysis of citric acid leads to the formation of H_2 along with CO_2 and C (Eq. 3), and at higher temperatures ($T > 700^\circ\text{C}$) pyrolysis of citric acid results into the generation of H_2 along with CO_2 , CO, and C (Eq. 4). Therefore, in this

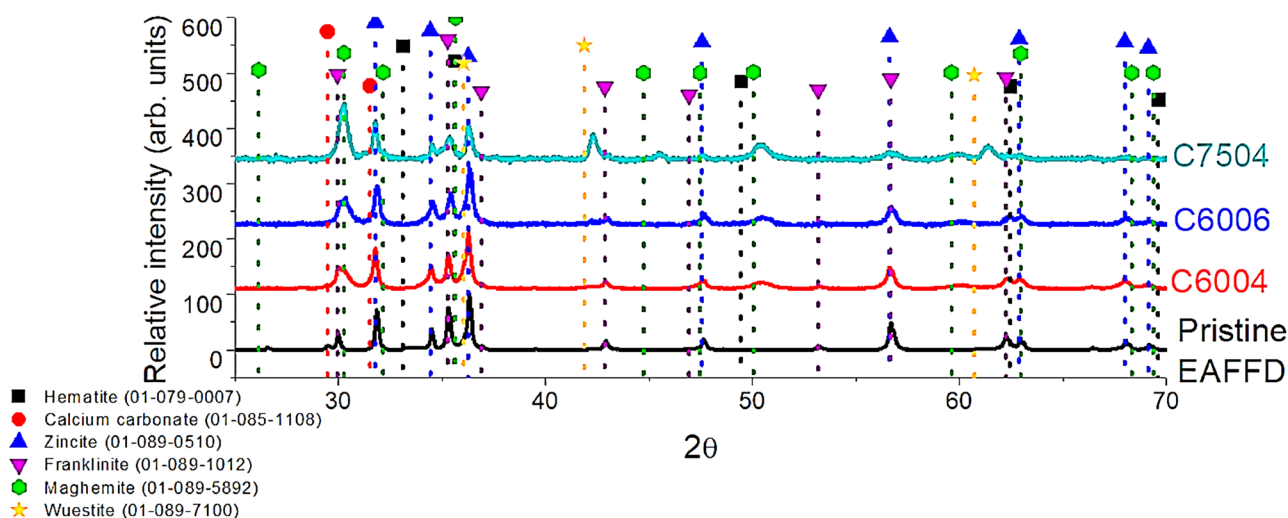
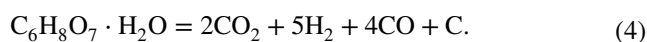
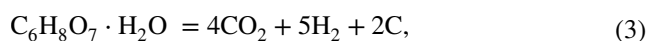
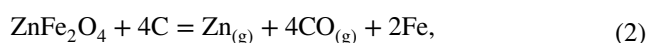
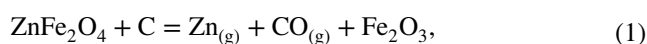


Fig. 2 XRD patterns of obtained powders

work, upon the application of pyrolysis at 600 °C franklinite may be partially reduced [37], while the forming carbon atoms generate a nanometer-thick carbon layer over the particles. Then, upon the application of pyrolysis at 750 °C, the formation of carbon monoxide (along with H₂) promotes a more remarkable phase transformation in the flue dust, accompanied by nanometer-thick C layer formation over the dust particles [27, 34]. Wu et al. [35] have reported that via heat treatment of the composite made of C and EAF flue dust, it is possible to get various structured iron oxides with the evaporation of zinc following the reduction of franklinite by CO [27] (Eqs. 1, 2). This fact could be ascribed to the formation of wuestite more remarkably on C7504, of which positions are shifted due to the fluorescence effect (seen in Fig. 2 and Figure S3).



When Raman spectra are examined in Fig. 3a–c, peaks at ~1330 cm⁻¹ and ~1580 cm⁻¹ refer to the D and G bands of carbon, respectively [38]. I_D/I_G ratios are calculated for C6004, C6006, and C7504 as 0.76, 0.79, and 0.89, respectively. Huang et al. [39] state that a lower I_D/I_G ratio leads to higher conductivity because of a better degree of order in the graphitized carbon. These results show that increasing pyrolysis duration and temperature results in higher I_D/I_G ratio, decreasing the physical properties of the powder.

HR-TEM is used to characterize C6004 in more detail (Fig. 4a–d). According to the general image (Fig. 4a–c), it is confirmed that the sample contains rod and spheres-like particles, as stated in the literature [22]. Figure 4b reveals the fractured edge of the nanorod following the mechanical activation process as well as C layer formation over the particle surface. EDS mapping (Figure S4) shows that the C6004 has additional Mn and Cr in its structures as agreed with XRF. Moreover, the nanometer-thick C layer is also detected in Fig. 4d. Lastly, SAED pattern (Figure S5 and Table S1) verifies existent phases in XRD analysis (Fig. 2).

Moreover, the carbon amount (wt%) in each sample is determined by Eltra CS800. The results show that around 2-wt% C is detected in the EAFFD, while the amount of C is found to be ~ 6 wt% for C6004 and C6006 and ~ 4 wt% for C7504 [36]. This fact verifies the explanation related to the phase transformation occurring in the electrode upon different pyrolysis conditions.

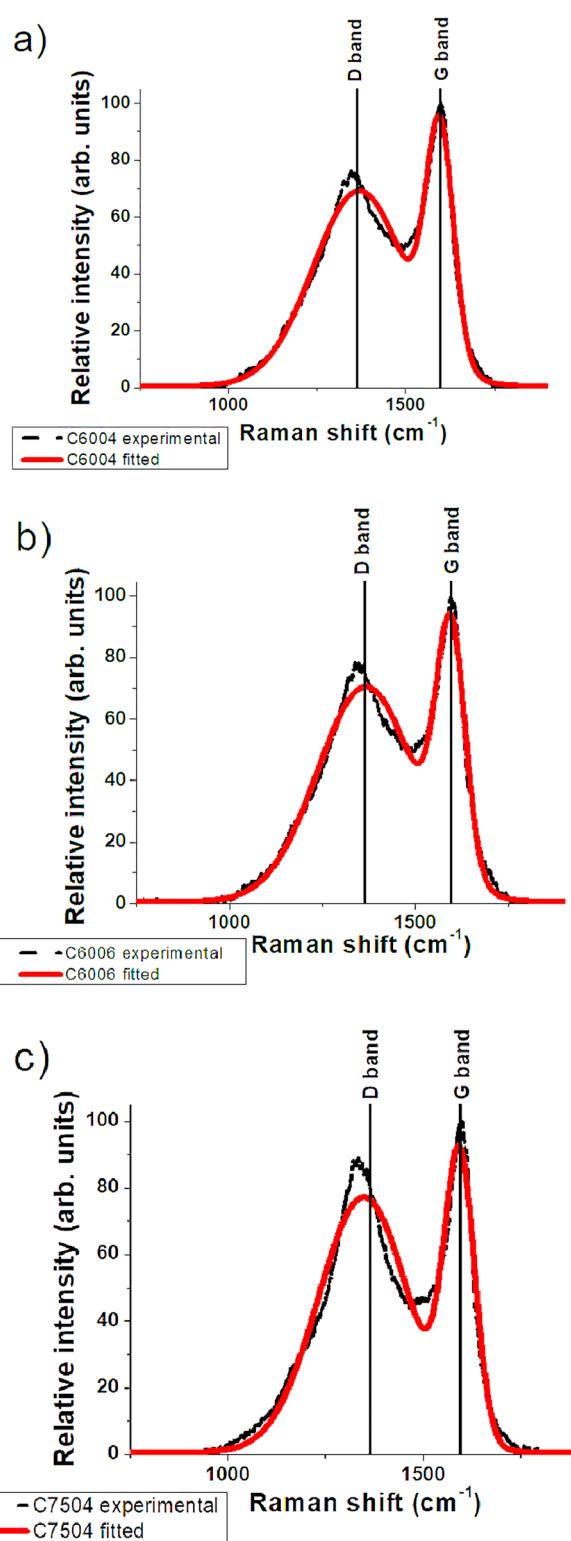


Fig. 3 Raman spectra of a C6004, b C6006, and c C7504

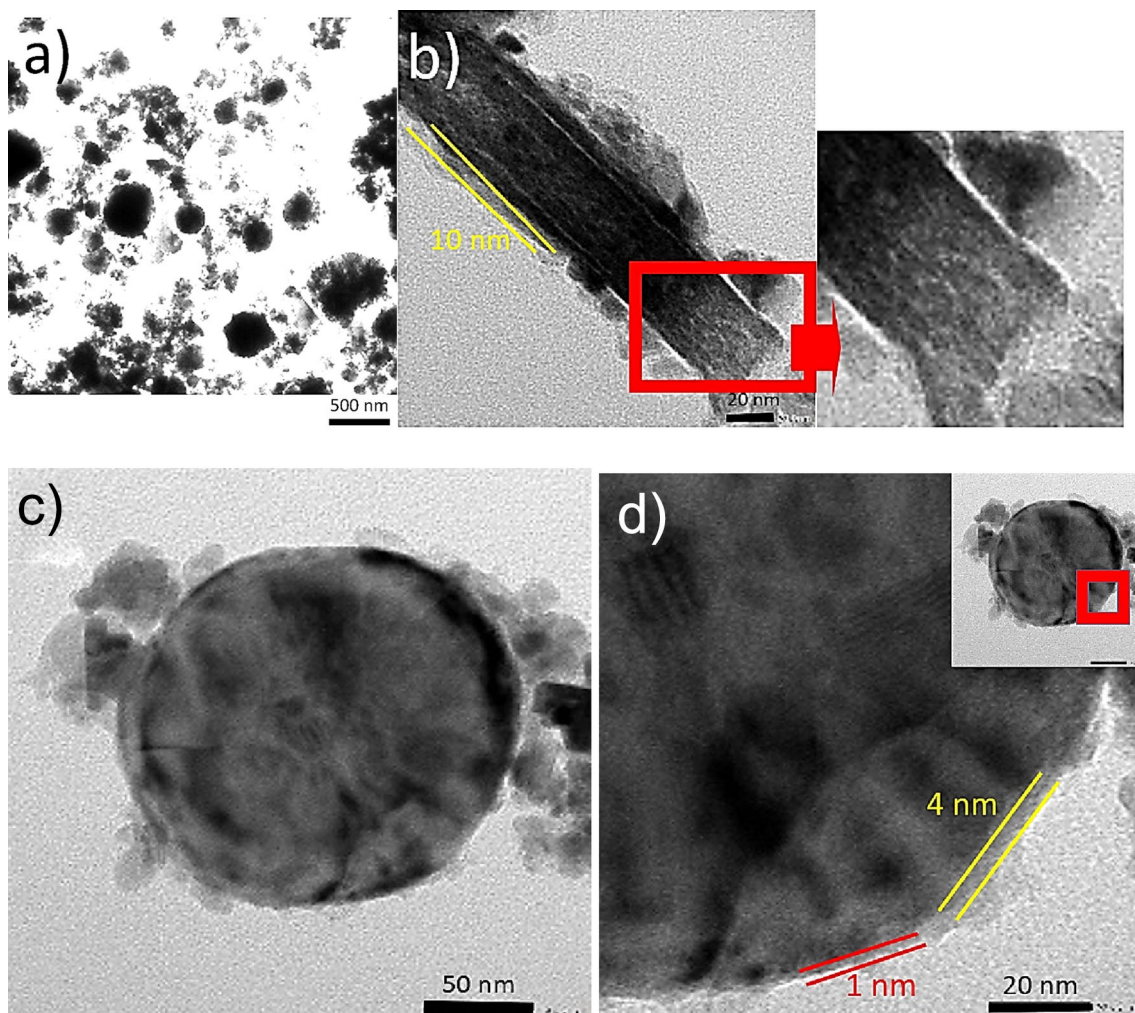


Fig. 4 HR-TEM images; **a** general image, **b** detailed investigation on rod-like particles, **c** a sphere-shaped particle, and **d** carbon layer on a spherical particle

Electrochemical Characterization

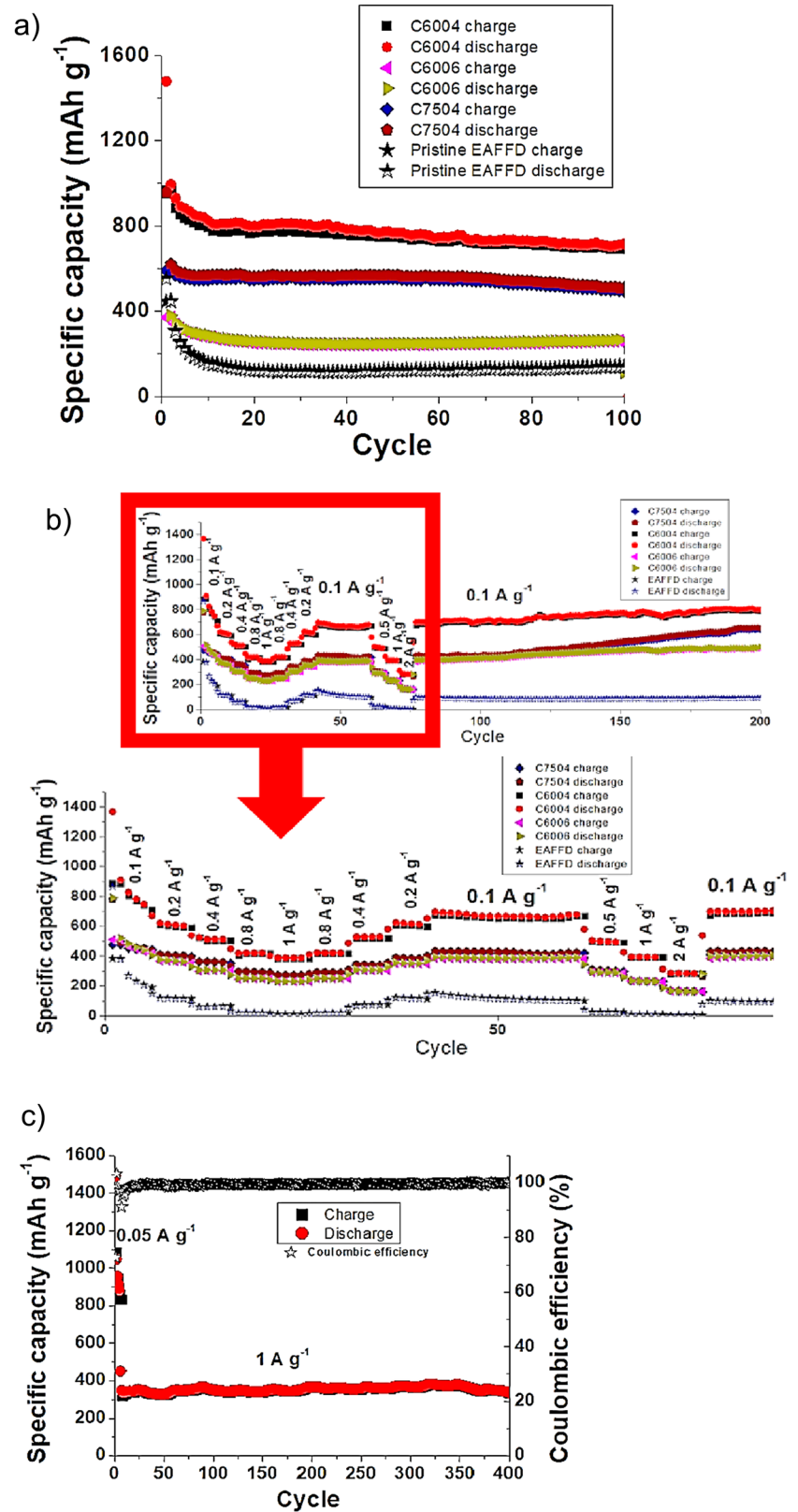
Galvanostatic tests are carried out under a current load of 50 mA g^{-1} (Fig. 5a): pure EAFFD demonstrates $\sim 550 \text{ mAh g}^{-1}$ discharge capacity in the first cycle and performs $\sim 20\%$ capacity retention over 100 cycles. Figure 5a shows that by C coating, the cycle performance of the EAFFD has been improved: C6004 delivers $\sim 1470 \text{ mAh g}^{-1}$ discharge capacity in the 1st cycle and reveals $\sim 50\%$ capacity retention over 100 cycles. C6006 demonstrates $\sim 570 \text{ mAh g}^{-1}$ discharge capacity in the 1st cycle and reveals $\sim 40\%$ capacity retention after 100 cycles. Lastly, C7504 performs 955 mAh g^{-1} discharge capacity in the 1st cycle and reveals $\sim 53\%$ capacity retention after 100 cycles.

Then, to evaluate the performance of each cell at different current loads ($0.1\text{-}0.2\text{-}0.4\text{-}0.8\text{-}1\text{-}0.8\text{-}0.4\text{-}0.2\text{-}0.1\text{-}0.5\text{-}1\text{-}2\text{-}0.1 \text{ A g}^{-1}$), rate tests are performed. Herein, C6004 reveals a very stable performance upon the increasing and decreasing

current loads. When a load of 0.1 A g^{-1} is applied to the sample, after being tested under a current load of 2 A g^{-1} , the electrode keeps delivering capacities similar to the 55th cycle, and performs $\sim 800 \text{ mAh g}^{-1}$ at the 200th cycle (Fig. 5b). Then for electrode stability assessment, an additional galvanostatic test is run where C6004 is cycled 3 times at 0.05 A g^{-1} , then 400 cycles at 1 A g^{-1} current loads. The result shows that C6004 delivers 380 mAh g^{-1} over 400 cycles. The retention from the 3rd to 400th cycle is 99.5% and the coulombic efficiency at the 400th cycle is 99.2% for C6004 when it is galvanostatically tested under a current load of 1 A g^{-1} . Such performance points up the remarkable stability of the electrode even under high current loads.

Figure 6a–d demonstrates the capacity–voltage curves of each electrode material for the first 3 cycles. The shape of the discharge curve is differentiated after the 1st cycle which proves that activation occurs in the first lithiation reaction as for the synthetic ZnFe_2O_4 anode material [40].

Fig. 5 Cycle performances of C6004, C6006, and C7504 between 1 mV and 3 V **a** under a current load of 50 mA g^{-1} , **b** under different current loads, and **c** galvanostatic test result of C6004 when it is tested under a current load of 1 A g^{-1} for 400 cycles



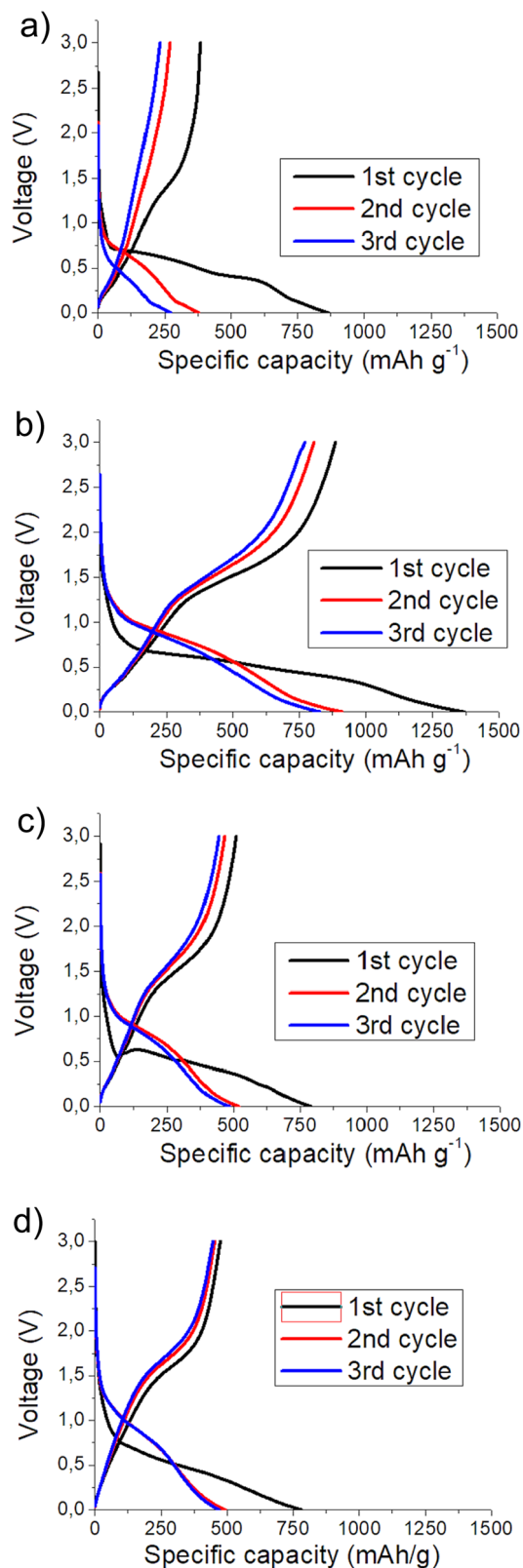
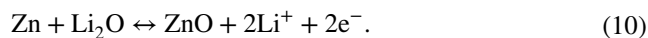
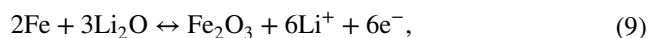
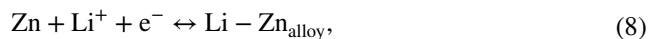
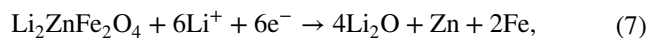
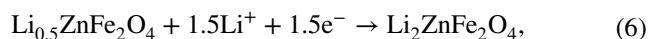
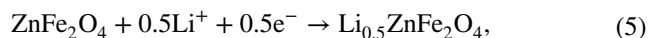


Fig. 6 Capacity–Voltage profile between 1 mV and 3 V at 100 mA g⁻¹; **a** pristine EAFDD, **b** C6004, **c** C6006, and **d** C7504

Ciambezi et al. [41] have proved that using in situ X-ray absorption spectroscopy (XAS) method, the synthetically fabricated ZnFe₂O₄ reaction with Li occurs in multi-steps with an initial activation process. Taking into consideration, previous studies where the lithiation of synthetically fabricated zincite is studied with in situ and ex situ characterization techniques (such as XRD, XAS), herein the lithiation mechanism is proposed as follows [42, 43]: Upon discharging, first 0.5 mol of Li is introduced into the ferrite structure around 1.5 V, resulting in a capacity of ~90 mAh g⁻¹ (Eq. 5). Then, the intermediate compound is transformed into Zn and Fe, upon further reduction (Eqs. 6 and 7). Additionally, down to 0.7 V the carbonate-based electrolyte is decomposed and solid electrolyte interface (SEI) forms on the electrode surface. Finally, further discharging results in the lithiation of Zn (Eq. 8). After this activation reaction, cycling occurs as defined in Eqs. 9 and 10 [40, 42, 44–47].



Next, EIS spectra of EAFDD and C6004 are examined (Fig. 7a, b). Symmetric cells have been assembled, as specified in the experimental part, to prevent the effect of impedance introduced by Li metal (counter electrode in the half-cell). Two depressed semicircles and an oblique line at low frequency are noticed on each of the spectra. They each relate to different processes, including the formation of SEI, the charge-transfer reaction at the electrolyte–electrode interface, and the diffusion of lithium ions throughout the electrode. The model used to fit experimental data is given in Fig. 7c. The results show that the C-coated EAFD (C6004) exhibits lower SEI (R8) and charge-transfer resistance (R10), indicating that their electrolyte–electrode complex reactions can occur easily (the R8 and R10 of C6004 are found to be 9.987 and 8.86, while the R8 and R10 of the EAFD are calculated as 30.81 and 38.11, respectively).

As the highest capacity is provided by C6004, sweep voltammetry is used at various sweep rates to distinguish between the effects of faradaic and non-faradaic reactions

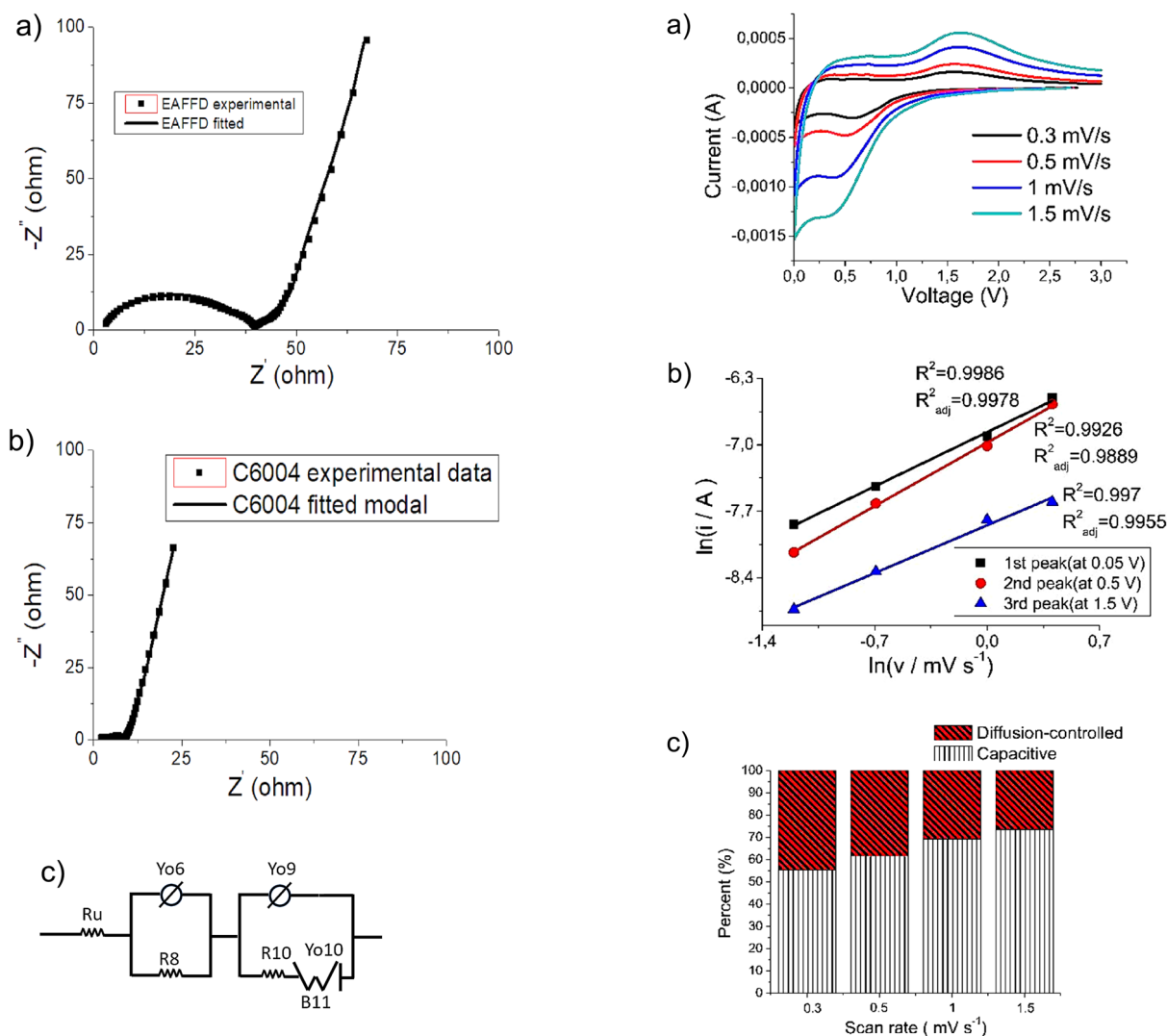


Fig. 7 EIS results and fitted model at 1 mV; **a** EAFFD, **b** C6004, and **c** fitted model

on the overall amount of Li stored in the lithiation reaction [29]. (As a reference, the EAFFD-pristine sample is also tested using the same procedure, and the result is reported in Figure S6 a–c). To stabilize the electrode/electrolyte interface, the electrode is first cycled 3 times at 100 mA g^{-1} between 1 mV and 3 V. Voltammetry is then used with varied scan speeds ranging from 1 mV to 3 V (Fig. 8a). Two cathodic peaks (at 0.05 and 0.5 V) and an anodic peak (at 1.52 V) are selected to calculate the capacitive contribution because they appear for all scan rates.

According to Duan et al. [29], the capacitive effect can be described using Eq. 11, where “a” is a constant referring to scan rate and “b” is a coefficient ranging from 0.5 to 1 (if b is close to 0.5, the reaction will be regulated by Li^+ diffusion, and if b is close 1 the capacitive effect will control the reaction). Figure 8b exhibits $\ln(\text{current})/\ln(\text{scan rate})$ chart. As

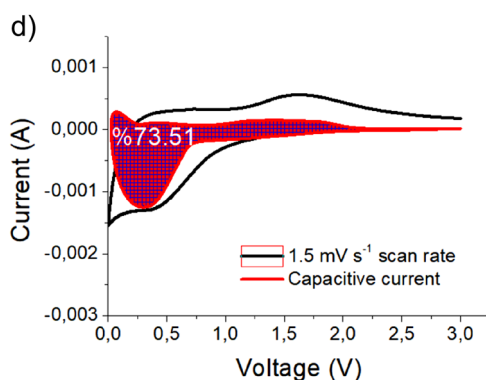


Fig. 8 **a** The CV loops of C6004 after testing at 100 mA g^{-1} between 1 mV and 3 V, **b** $\ln(\text{current})$ vs $\ln(\text{sweep rate})$ plot of C6004, **c** Capacity contribution of C6004 at various scan rates, and **d** Capacitive contributions at 1.5 mV s^{-1}

a result, the b value of C6004 has been found to be 0.8278. This means that carbon in the active material enhances the capacitive contribution (Fig. 8d). The prevalence of this capacitive effect at different scan rates is noted in Fig. 8c.

$$k_1 \times v + k_2 \times v^{\frac{1}{2}} = a.v^b. \quad (11)$$

Finally, *ex situ* SEM analyses are done for each electrode after 1st discharge (at 1 mV vs Li/Li⁺) and 1st charge (at 3 V vs Li/Li⁺) reactions to reveal the reason for the differentiation in their cycle performances. No severe delamination/peeling is noted for any of the electrodes which prove that laminations are realized successfully. Figure 9a shows that upon the 1st discharge of EAFFD electrode, high volumetric expansion occurs dramatically and the lamination gets wrinkled. Close examination reveals that spherical particles (i.e., ferrite) are swollen when the electrode is discharged down to 1 mV and then upon charging up to 3 V (vs Li), the swollen particles are noted to partially retain their morphology (Fig. 9b). This could be related to the low Li diffusion kinetic of the electrode material, as verified by its low-rate performance (Fig. 5b). Moreover, when the first discharge morphologies of the C-coated electrodes (C6004, C6006, and C7504) are compared to that of the EAF electrode, any of them demonstrate wrinkles in their laminations which might be related to the buffering effect of C atoms present in the electrode active material. Then, Fig. 9c shows that for C6004, once the electrode is discharged down to 1 mV no micron-sized spheres are detected on the electrode surface, instead following the activation reaction, the spheres made of ferrite are transformed into metal nanoparticles. Thanks to these nano-sized particles, a more stable electrode/electrolyte interface (Fig. 9d) is obtained which leads to better cycling efficiency (Fig. 5a–c).

On the other hand, the *ex situ* SEM image of C6006 depicts those swollen spherical particles appear at 1 mV, and these structures did not fully recover their initial morphologies and sizes when the electrode is charged to 3 V (vs Li). A close investigation also determines fractures on the C6006 surface when it is charged to 3 V (Fig. 9e, f). The latter could be the reason for the lower cycle performance of this sample (in comparison to C6004, Fig. 5a, b). Finally, Fig. 9g and h demonstrates that in case of C7504, at 1 mV, no micron-sized spherical particles are detected at 1 mV and at 3 V which proves that activation occurs and transformation of franklinite structure is realized in the sample. However, upon close examination, it is seen that Li's removal from C7504 creates cracks in the electrode which may be related to the low C content in the active electrode material (in comparison to C6004, Fig. 5a, b).

In conclusion, the difference in the structural and morphological properties of each powder (as revealed by SEM and XRD results) as well as the dissimilarity in C amount

can explain the variations in the galvanostatic performances of C6004, C6006, and C7504. The superior performance of C6004 is believed to be related to the synergetic effect of its complex composition, optimized C film features, and the presence of doped elements in the oxide structures which promote Li diffusion upon cycling [42].

Conclusion

Previously, studies on Zinc recovery from EAFFD through high temperature and/or energy expenditure were published. Unlikely, in this study, a new strategy has been put forward to propose solutions for the future energy crisis as well as the environmental problems (such as waste storage). To develop and demonstrate this concept, a combination of ball milling and pyrolysis was investigated, in which citric acid was used as a carbon source in milling and pyrolysis was performed under various conditions (temperatures and durations) to optimize the cycle performance of the anode material.

- Characterizations show that during milling and pyrolysis, remarkable changes occurred in the structure and the morphology of each powder,
- TEM investigation reveals that a nanometer-thick carbon layer is present over the particle surface of C6004, after pyrolysis.
- Galvanostatic tests depict that C6004 performs the best performance: It delivers 1477.23 mAh g⁻¹ initially and retains 50% of it after the 100th cycle, when it is tested under a current load of 50 mA g⁻¹. Then, C6004 delivers 380 mAh g⁻¹ capacity over 400 cycles with 99.2% coulombic efficiency when it is cycled under a current load of 1 A g⁻¹.

This work has conclusively demonstrated that high-performance electrodes may be produced utilizing secondary production methods that employ sustainable engineering methodologies rather than synthetic production processes that require high investment costs and generate significant CO₂. The current method for valorizing industrial waste in a high value-added application is likely to serve as a model for 'trash to treasure.'

Supplementary Information The online version contains supplementary material available at <https://doi.org/10.1007/s40831-024-00801-w>.

Acknowledgements The author acknowledges Istanbul Medipol University as this project is financially supported by Istanbul Medipol University Scientific Research Projects Program (Project no: 2020/20). The author thanks Resul Tatlı (EMPET Metalurji San. ve Tic. Ltd. Şti.) for supplying the raw material and electric arc furnace dust. The authors thank Dr. Alper Yeşilçubuk, Dr. Havva Kazdağ, Dr. Hüseyin Aydın, and Yasemin Kılıç for their help in the characterizations.

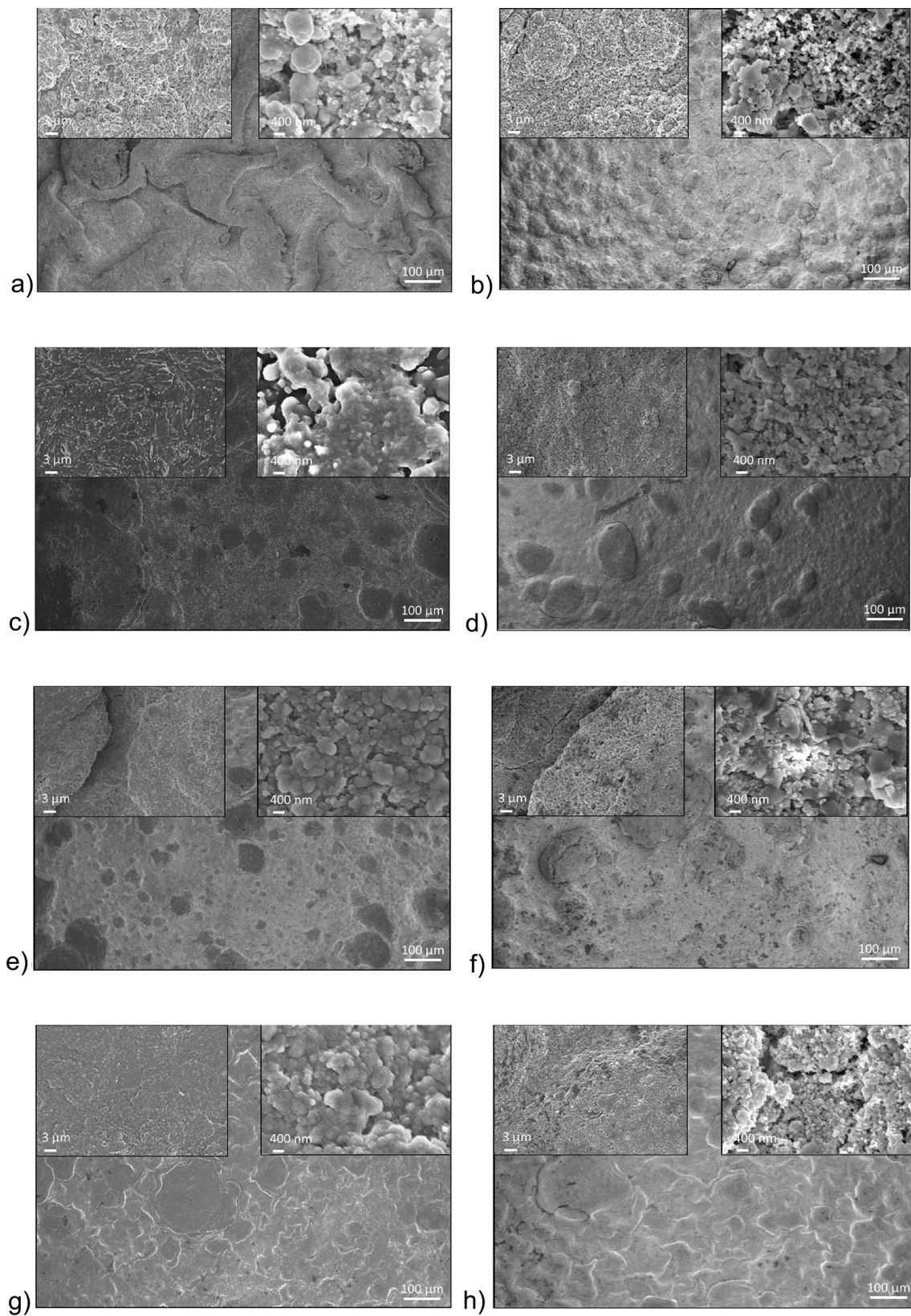


Fig. 9 Ex situ SEM micrographs when the electrodes are discharged down to 1 mV vs Li: **a** EAF, **c** C6004, **e** C6006, and **g** C7504. Ex situ SEM micrographs when the electrodes are charged to 3 V vs Li: **b** EAF, **d** C6004, **f** C6006, and **h** C7504

Funding Open access funding provided by the Scientific and Technological Research Council of Türkiye (TÜBİTAK).

Declarations

Conflict of interest Billur Deniz Karahan reports that a financial support was provided by Istanbul Medipol University (Project no: 2020/20). Billur Deniz Karahan used to work at Istanbul Medipol University which sponsored the realization and characterization of the experiments. Istanbul Technical University is the current affiliation of the corresponding author.

Open Access This article is licensed under a Creative Commons Attribution 4.0 International License, which permits use, sharing, adaptation, distribution and reproduction in any medium or format, as long as you give appropriate credit to the original author(s) and the source, provide a link to the Creative Commons licence, and indicate if changes were made. The images or other third party material in this article are included in the article's Creative Commons licence, unless indicated otherwise in a credit line to the material. If material is not included in the article's Creative Commons licence and your intended use is not permitted by statutory regulation or exceeds the permitted use, you will need to obtain permission directly from the copyright holder. To view a copy of this licence, visit <http://creativecommons.org/licenses/by/4.0/>.

References

- Orfanos N, Mitzelos D, Sagani A, Dedoussis V (2019) Life-cycle environmental performance assessment of electricity generation and transmission systems in Greece. *Renew Energy* 139:1447–1462. <https://doi.org/10.1016/j.renene.2019.03.009>
- Kurzweil P, Garche J (2017) Overview of batteries for future automobiles. Elsevier, Amsterdam
- Orangi S, Manjong N, Clos DP et al (2024) Historical and prospective lithium-ion battery cost trajectories from a bottom-up production modeling perspective. *J Energy Storage*. <https://doi.org/10.1016/j.est.2023.109800>
- Nitta N, Wu F, Lee JT, Yushin G (2015) Li-ion battery materials: present and future. *Mater Today* 18:252–264. <https://doi.org/10.1016/j.mattod.2014.10.040>
- Li M, Lu J, Chen Z, Amine K (2018) 30 Years of lithium-ion batteries. *Adv Mater* 30:1–24. <https://doi.org/10.1002/adma.20180561>
- Kali R, Padya B, Rao TN, Jain PK (2019) Solid waste-derived carbon as anode for high performance lithium-ion batteries. *Diam Relat Mater* 98:107517. <https://doi.org/10.1016/j.diamond.2019.107517>
- Fichtner M, Edström K, Ayerbe E et al (2022) Rechargeable batteries of the future—the state of the art from a BATTERY 2030+ perspective. *Adv Energy Mater*. <https://doi.org/10.1002/aenm.202102904>
- Ziegler MS, Song J, Trancik JE (2021) Determinants of lithium-ion battery technology cost decline. *Energy Environ Sci* 14:6074–6098. <https://doi.org/10.1039/d1ee01313k>
- Wang J, Zhang Y, Cui K et al (2021) Pyrometallurgical recovery of zinc and valuable metals from electric arc furnace dust—a review. *J Clean Prod* 298:126788. <https://doi.org/10.1016/j.jclepro.2021.126788>
- Wu H, Zheng L, Zhan J et al (2020) Recycling silicon-based industrial waste as sustainable sources of Si/SiO₂ composites for high-performance Li-ion battery anodes. *J Power Sour* 449:227513. <https://doi.org/10.1016/j.jpowsour.2019.227513>
- Gao SW, Gong XZ, Liu Y, Zhang QQ (2018) Energy consumption and carbon emission analysis of natural graphite anode material for lithium batteries. *Mater Sci Forum* 913:985–990. <https://doi.org/10.4028/www.scientific.net/MSF.913.985>
- Engels P, Cerdas F, Dettmer T et al (2022) Life cycle assessment of natural graphite production for lithium-ion battery anodes based on industrial primary data. *J Clean Prod* 336:130474. <https://doi.org/10.1016/j.jclepro.2022.130474>
- WorldSteel Association (2022) Press Release – December 2021 crude steel production and 2021 global crude steel production totals, pp 1–5
- Fan Z, Friedmann SJ (2021) Low-carbon production of iron and steel: Technology options, economic assessment, and policy. *Joule* 5:829–862. <https://doi.org/10.1016/j.joule.2021.02.018>
- Rudnik E (2020) Recovery of zinc from steelmaking flue dust by hydrometallurgical route. *Arch Metall Mater* 65:601–608
- Ruiz O, Clemente C, Alonso M, Alguacil FJ (2007) Recycling of an electric arc furnace flue dust to obtain high grade ZnO. *J Hazard Mater* 141:33–36. <https://doi.org/10.1016/j.jhazmat.2006.06.079>
- Halli P, Hamuyuni J, Leikola M, Lundström M (2018) Developing a sustainable solution for recycling electric arc furnace dust via organic acid leaching. *Miner Eng* 124:1–9. <https://doi.org/10.1016/j.mineng.2018.05.011>
- Rahayu DS, Kusumastuti Y, Astuti W et al (2023) Recycling of electric arc furnace dust waste as a precursor in pharmaceutical grade zinc oxide synthesis. *Circ Econ Sust*. <https://doi.org/10.1007/s43615-023-00284-z>
- Darezereshki E, Vakylabad AB, Koohestani B (2021) A Hydrometallurgical approach to produce nano-ZnO from electrical arc furnace dusts. *Min Metall Explor* 38:1525–1535. <https://doi.org/10.1007/s42461-021-00412-z>
- Jin R, Liu J, Qiu H et al (2020) Synthesis of porous nanosheet-assembled ZnFe₂O₄@polypyrrole yolk-shell microspheres as anode materials for high-rate lithium-ion batteries. *J Electroanal Chem* 863:114038. <https://doi.org/10.1016/j.jelechem.2020.114038>
- Te HC, Lin CY, Chen YF, Lin JS (2013) Synthesis of ZnO@Graphene composites as anode materials for lithium ion batteries. *Electrochim Acta* 111:359–365. <https://doi.org/10.1016/j.electacta.2013.07.197>
- Karahan BD (2022) Carbon coated electric arc furnace dust prepared by one-pot pyrolysis: an efficient, low carbon footprint electrode material for lithium-ion batteries. *Mater Chem Phys* 287:126178. <https://doi.org/10.1016/j.matchemphys.2022.126178>
- Wang K, Cai R, Yuan T et al (2009) Process investigation, electrochemical characterization and optimization of LiFePO₄/C composite from mechanical activation using sucrose as carbon source. *Electrochim Acta* 54:2861–2868. <https://doi.org/10.1016/j.electacta.2008.11.012>
- Nzababimana J, Liu Z, Guo S et al (2020) Top-down synthesis of silicon/carbon composite anode materials for lithium-ion batteries: mechanical milling and etching. *Chemsuschem* 13:1923–1946
- Ng SH, Wang J, Wexler D et al (2007) Amorphous carbon-coated silicon nanocomposites: a low-temperature synthesis via spray pyrolysis and their application as high-capacity anodes for lithium-ion batteries. *J Phys Chem C* 111:11131–11138. <https://doi.org/10.1021/jp072778d>
- Yang H, Zhu HL, Qi YX et al (2020) Optimizing the cycling life and high-rate performance of Li₂ZnTi₃O₈ by forming thin uniform carbon coating derived from citric acid. *J Mater Sci* 55:15538–15550. <https://doi.org/10.1007/s10853-020-04980-1>
- Wang J, Liu XM, Yang H, Shen XD (2011) Characterization and electrochemical properties of carbon-coated Li₄Ti₅O₁₂ prepared by a citric acid sol-gel method. *J Alloys Compds* 509:712–718. <https://doi.org/10.1016/j.jallcom.2010.07.215>

28. Chen CH, Liu J, Amine K (2001) Symmetric cell approach and impedance spectroscopy of high power lithium-ion batteries. *J Power Sour* 96:321
29. Duan H, Du L, Zhang S et al (2019) Superior lithium-storage properties derived from a high pseudocapacitance behavior for a peony-like holey Co₃O₄ anode. *J Mater Chem A* 7:8327–8334. <https://doi.org/10.1039/c9ta00294d>
30. Kashif I, Soliman AA, Sakr EM, Ratep A (2013) XRD and FTIR studies the effect of heat treatment and doping the transition metal oxide on LiNbO₃ and LiNb₃O₈ nano-crystallite phases in lithium borate glass system. *Spectrochim Acta—Part A Mol Biomol Spectrosc* 113:15–21. <https://doi.org/10.1016/j.saa.2013.04.084>
31. Machado JGMS, Brehm FA, Moraes CAM et al (2006) Chemical, physical, structural and morphological characterization of the electric arc furnace dust. *J Hazard Mater* 136:953–960. <https://doi.org/10.1016/j.jhazmat.2006.01.044>
32. Chairaksa-Fujimoto R, Inoue Y, Umeda N et al (2015) New pyrometallurgical process of EAF dust treatment with CaO addition. *Int J Miner Metall Mater* 22:788–797. <https://doi.org/10.1007/s12613-015-1135-6>
33. Chaturvedi S, Dave PN (2012) Nano-metal oxide: potential catalyst on thermal decomposition of ammonium perchlorate. *J Exp Nanosci* 7:205–231. <https://doi.org/10.1080/17458080.2010.517571>
34. Holloway PC, Etsell TH, Murland AL (2008) Modification of Waelz kiln processing of La Oroya zinc ferrite. *Miner Metall Process* 25:97–104. <https://doi.org/10.1007/bf03403393>
35. Wu CC, Chang FC, Chen WS et al (2014) Reduction behavior of zinc ferrite in EAF-dust recycling with CO gas as a reducing agent. *J Environ Manag* 143:208–213. <https://doi.org/10.1016/j.jenvman.2014.04.005>
36. Barbooti MM, Al-Sammerrai DA (1986) Thermal decomposition of citric acid. *Thermochim Acta* 98:119–126. [https://doi.org/10.1016/0040-6031\(86\)87081-2](https://doi.org/10.1016/0040-6031(86)87081-2)
37. Polsilapa S, Sadedin DR, Wangyao P (2012) Thermodynamics analysis for the zinc ferrite reduction by hydrogen. *High Temp Mater Process* 30:587–592. <https://doi.org/10.1515/htmp.2011.119>
38. Puech K, Paredes et al (2019) Analyzing the Raman Spectra of graphenic carbon materials from kerogens to nanotubes: what type of information can be extracted from defect bands? *C—J Carbon Res.* <https://doi.org/10.3390/c5040069>
39. Huang X, Du Y, Qu P et al (2017) Effect of carbon coating on the properties and electrochemical performance of LiFePO₄/C composites by vacuum decomposition method. *Int J Electrochem Sci* 12:7183–7196
40. Bini M, Ambrosetti M, Spada D (2021) ZnFe₂O₄, a green and high-capacity anode material for lithium-ion batteries: a review. *Appl Sci.* <https://doi.org/10.3390/app112411713>
41. Ciambezi M, Trapananti A, Rezvani SJ et al (2020) Initial lithiation of carbon-coated zinc ferrite anodes studied by in-situ X-ray absorption spectroscopy. *Radiat Phys Chem* 175:108468. <https://doi.org/10.1016/j.radphyschem.2019.108468>
42. Bresser D, Mueller F, Fiedler M et al (2013) Transition-metal-doped zinc oxide nanoparticles as a new lithium-ion anode material. *Chem Mater* 25:4977–4985. <https://doi.org/10.1021/cm403443t>
43. Trapananti A, Eisenmann T, Giuli G et al (2021) Isovalent vs. aliovalent transition metal doping of zinc oxide lithium-ion battery anodes — in-depth investigation by ex situ and operando X-ray absorption spectroscopy. *Mater Today Chem* 20:100478
44. Ding Y, Yang Y, Shao H (2011) High capacity ZnFe₂O₄ anode material for lithium ion batteries. *Electrochim Acta* 56:9433–9438. <https://doi.org/10.1016/j.electacta.2011.08.031>
45. Hwang H, Shin H, Lee WJ (2017) Effects of calcination temperature for rate capability of triple-shelled ZnFe₂O₄ hollow microspheres for lithium ion battery anodes. *Sci Rep* 7:1–10. <https://doi.org/10.1038/srep46378>
46. Wu G, Jia Z, Cheng Y et al (2019) Easy synthesis of multi-shelled ZnO hollow spheres and their conversion into hedgehog-like ZnO hollow spheres with superior rate performance for lithium ion batteries. *Appl Surf Sci* 464:472–478. <https://doi.org/10.1016/j.apsusc.2018.09.115>
47. Liu T, Guo Y, Hou S et al (2021) Constructing hierarchical ZnO@C composites using discarded Sprite and Fanta drinks for enhanced lithium storage. *Appl Surf Sci* 541:148495. <https://doi.org/10.1016/j.apsusc.2020.148495>

Publisher's Note Springer Nature remains neutral with regard to jurisdictional claims in published maps and institutional affiliations.

Authors and Affiliations

Mehmet Feryat Gülcan¹ · Billur Deniz Karahan^{1,2}

✉ Billur Deniz Karahan
bdkarahan@itu.edu.tr

¹ Department of Metallurgical and Materials Engineering, Istanbul Technical University, Ayazaga Campus, 34469 Istanbul, Turkey

² Research Institute for Health Sciences and Technologies (SABITA), Istanbul Medipol University, 34810 Beykoz-Istanbul, Turkey